



LAWRENCE
LIVERMORE
NATIONAL
LABORATORY

A Superconducting Tunnel Junction X-ray Spectrometer without Liquid Cryogenes

S. Friedrich, T. Hertrich, O. B. Drury, N. J. Cherepy, J. Hohne

June 24, 2008

Symposium on Radiation Measurements and Applications
Berkeley, CA, United States
June 2, 2008 through June 5, 2008

Disclaimer

This document was prepared as an account of work sponsored by an agency of the United States government. Neither the United States government nor Lawrence Livermore National Security, LLC, nor any of their employees makes any warranty, expressed or implied, or assumes any legal liability or responsibility for the accuracy, completeness, or usefulness of any information, apparatus, product, or process disclosed, or represents that its use would not infringe privately owned rights. Reference herein to any specific commercial product, process, or service by trade name, trademark, manufacturer, or otherwise does not necessarily constitute or imply its endorsement, recommendation, or favoring by the United States government or Lawrence Livermore National Security, LLC. The views and opinions of authors expressed herein do not necessarily state or reflect those of the United States government or Lawrence Livermore National Security, LLC, and shall not be used for advertising or product endorsement purposes.

A Superconducting Tunnel Junction X-ray Spectrometer without Liquid Cryogenics

Stephan Friedrich, Theo Hertrich, Owen B. Drury, Nerine J. Cherepy, Jens Höhne

Abstract—Superconducting tunnel junctions (STJs) are being developed as X-ray detectors because they combine the high energy resolution of cryogenic detector technologies with the high count rate capabilities of athermal devices. We have built STJ spectrometers for chemical analysis of dilute samples by high-resolution soft X-ray spectroscopy at the synchrotron. The instruments use 36 pixels of $200\text{ }\mu\text{m} \times 200\text{ }\mu\text{m}$ Nb-Al-AlOx-Al-Nb STJs with 165 nm thick Nb absorber films. They have achieved an energy resolution of $\sim 10 - 20\text{ eV}$ FWHM for X-ray energies below 1 keV, and can be operated at a total count rate of $\sim 10^6$ counts/s. For increased user-friendliness, we have built a liquid-cryogen-free refrigerator based on a two-stage pulse tube cryocooler in combination with a two-stage adiabatic demagnetization stage. It holds the STJ detector at the end of a 40-cm-long cold finger, and attains the required operating temperature of $\sim 0.3\text{ K}$ at the push of a button. We describe the instrument performance and present speciation measurements on Eu dopant activators in the novel scintillator material SrI_2 to illustrate the potential for STJ spectrometers at the synchrotron.

Index Terms— Superconducting devices, STJ X-ray detector, cooling, pulse tube refrigerator, adiabatic demagnetization, strontium iodide

I. INTRODUCTION

CRYOGENIC photon and particle detectors with operating temperatures below 1 K are being developed for scientific and technological applications because of the high energy resolution and high sensitivity that low-temperature operation enables [1]. Among the different detector technologies, superconducting tunnel junction (STJ) charge detectors are distinguished by their speed and high count rate capabilities of several 10,000 counts/s per detector pixel, because charge transport in STJs is fast compared to phonon transport in thermal microcalorimeter detectors. This typically comes at the expense of a lower energy resolution for STJs than for microcalorimeters, since STJ detectors must be

operated at $T \ll T_C$ so that at a given temperature energies to create signal carriers are higher for excess charges than for excess phonons. STJs are therefore preferred in applications that require higher energy resolution than conventional Si(Li) or Ge detectors can offer, and higher count rate capabilities than microcalorimeters. This includes, for example, high-resolution soft X-ray spectroscopy at synchrotron light sources [2].

The widespread applications of STJ spectrometers in X-ray spectroscopy depends in part on making this technology available to general users who are typically not experts in low temperature physics. We have therefore built a refrigerator that can attain the required STJ operating temperatures of $\sim 0.5\text{ K}$ or below without the use of cryogenic liquids. The instrument is designed for STJ X-ray operation at the synchrotron, and therefore holds the STJ detector at the end of a cold finger that can be inserted into the UHV chamber of typical endstations. Here we describe the instrument performance, and illustrate its potential in material science with an X-ray analysis of europium dopants in novel SrI_2 scintillator materials.

II. SUPERCONDUCTING TUNNEL JUNCTION X-RAY DETECTORS

A. Design

Superconducting tunnel junctions (STJs) consist of two superconducting electrodes separated by a thin insulating tunneling barrier. X-ray absorption in one of the electrodes breaks the Cooper pairs of the superconducting ground state and excites free excess charge carriers (“quasiparticles”) in proportion to the X-ray energy E_x above the superconducting energy gap Δ . As these quasiparticles tunnel through the barrier at a rate $1/\tau_{\text{tun}}$, they generate a temporary increase in tunneling current that can be directly read out with an FET-based preamplifier at room temperature (figure 1). The high energy resolution in STJs is due to the fact that the energy $\epsilon = 1.7\Delta$ to create an excess charge, where the factor 1.7 accounts for the partial energy loss to phonons, scales with the energy gap Δ . For superconductors, Δ is of order 1 meV and thus a factor ~ 1000 smaller than in semiconductors, giving rise to an improved energy resolution by a factor $\sqrt{1000} \approx 30$ [3].

STJ electrodes typically consist of a superconducting bilayer with a thick absorber with large energy gap Δ_{abs} for high efficiency, and a thin trapping layer with small energy gap Δ_{trap} for fast tunneling. Quasiparticles from the absorber are trapped into the lower-gap region by inelastic scattering, and the small trap thickness ensures fast tunneling [4].

Manuscript received June 2, 2008. This work was supported by the National Aeronautics and Space Administration under NASA ASTID grant L-10896, and by the U.S. Department of Energy, Office of Non-Proliferation Research NA-22. We thank the ALS synchrotron for beam time at beam line 4.0.2. The work was performed under the auspices of the U.S. Department of Energy by Lawrence Livermore National Laboratory under Contract DE-AC52-07NA27344.

S. Friedrich and O. B. Drury are with the Advanced Detector Group at Lawrence Livermore National Laboratory, Livermore, CA 94550 (phone: +1-925-423-1527; fax: +1-925-422-7310; e-mail: friedrich1@llnl.gov).

T. Hertrich and J. Höhne are with VeriCold Technologies GmbH, 85737 Ismaning, Germany (e-mail: jens.hoehne@vericold.com).

N. J. Cherepy is with the Chemistry and Material Sciences Directorate at Lawrence Livermore National Laboratory, Livermore, CA 94550 (e-mail: cherepy1@llnl.gov).

Quasiparticles can tunnel multiple times by forward tunneling into the counterelectrode (figure 1, process 1), or by “backtunneling”, i.e. by breaking Cooper pairs in the opposite electrode (figure 1, process 2). Each time they transfer charge in the *same* direction as the forward tunneling process, until they eventually form Cooper pairs again after a recombination time τ_{rec} . Backtunneling produces an intrinsic gain by a factor $\langle n \rangle = \tau_{rec}/\tau_{tun}$ equal to the average number $\langle n \rangle$ of tunneling events for each quasiparticle [5]. In addition, quasiparticles that remain in the traps at energies $>eV_{bias}$ above the energy gap Δ_{trap} can also tunnel *against* the bias, this time *reducing* the signal charge transfer (figure 1, process 3) [6]. This process occurs with a probability γ and is suppressed when quasiparticles scatter below eV_{bias} . The total signal charge therefore depends on the relative time scales for tunneling, inelastic scattering and recombination in the electrodes.

The fundamental limit to the energy resolution of STJs is given by the statistical variations in quasiparticle generation and tunneling according to

$$\Delta E_{FWHM} \approx 2.355 \sqrt{1.7\Delta \cdot E \left(F + 1 + \frac{1}{\langle n \rangle} + \frac{4\gamma(1-\gamma)}{(1-2\gamma)^2} \right)} \quad (1)$$

Here $F = 0.2$ is the Fano factor that describes the statistical fluctuations of the initial quasiparticle generation process [3], and $1+1/\langle n \rangle$ describes the fluctuations in the number $\langle n \rangle$ of tunneling events that each quasiparticle undergoes [5]. The γ -dependent factor describes the statistical fluctuations due to the partitioning of charge transfer processes with and against the bias [6]. In the limit of strong backtunneling ($\langle n \rangle \rightarrow \infty$) and fast trapping by inelastic scattering ($\gamma \rightarrow 0$), Nb-based STJs ($\Delta_{Nb} = 1.5$ meV) can have an energy resolution between 0.13 eV and 4.3 eV FWHM for photon energies between 1 eV and 1 keV. For lower-gap Ta ($\Delta_{Ta} = 0.7$ meV) or Hf ($\Delta_{Hf} = 0.02$ meV), this limit improves to 0.04 or 0.015 eV at 1 eV, and 2.8 eV or 0.5 eV at 1 keV.

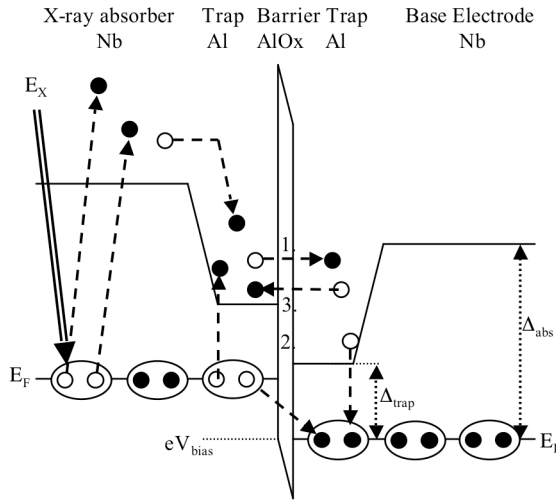


Fig. 1. Band diagram $\Delta(x)$ inside an STJ X-ray detector. Charges created in the absorber with gap Δ_{abs} diffuse into the low-gap region with Δ_{trap} and are trapped by inelastic scattering. They produce a current signal by tunneling (process 1), backtunneling (process 2) and reverse tunneling (process 3).

The maximum STJ count rates are determined by the recombination time τ_{rec} that the quasiparticles remain in the electrodes before they recombine into the superconducting ground state and again form Cooper pairs. This recombination time is typically in the microsecond range, and enables STJ detector operation at rates up to several 10,000 counts/s per detector pixel [7, 8].

B. Performance

Our STJ detectors based on Nb-Al-AlOx-Al-Nb tunnel junctions have attained an energy resolution between 4.5 and 8.9 eV FWHM in the soft X-ray band between 0.2 and 1 keV [9]. For Ta-based STJs with lower energy gap and higher film quality, an energy resolution of 2.55 eV FWHM at 0.4 keV and 6.3 eV FWHM at 1.82 keV has been measured [10]. STJ operation can be extended to higher energies by adding a 2 μ m Pb absorber, with the best energy resolution at 6 keV around 12 eV FWHM [11].

Nb-based STJs tend to have relatively short quasiparticle recombination times τ_{rec} , possibly because of the formation of NbO suboxides along Nb grain boundaries that serve as trapping and recombination sites [12]. Our STJ detectors with $\tau_{rec} \sim 3$ μ s can be operated at $>20,000$ counts/s per pixel at maximum energy resolution [7], and up to 100,000 counts/s for shorter shaping times if the associated degradation in energy resolution to ~ 40 eV is acceptable (figure 2) [8]. Ta-based devices tend to have longer recombination times, typically ~ 30 μ s, allowing maximum count rates of ~ 3500 counts/s per pixel without loss in energy resolution [12].

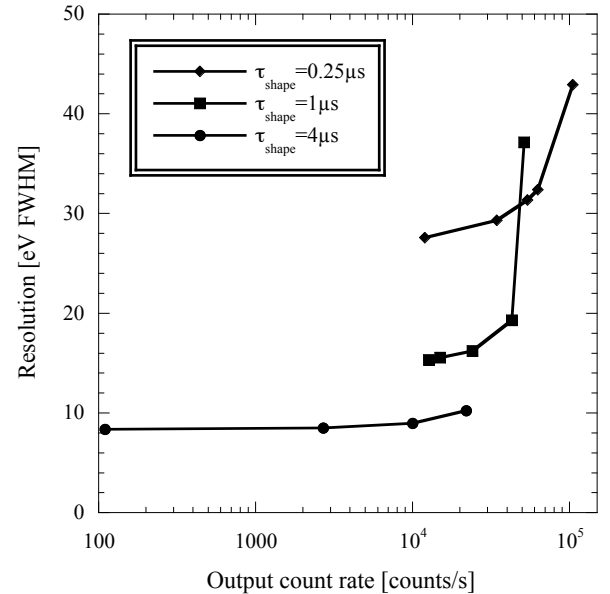


Fig. 2. Energy resolution of a Nb-Al-AlOx-Al-Nb STJ detector as a function of count rate for different shaping times at an energy of 277 eV [8].

III. CRYOSTAT DESIGN

Although superconducting X-ray detectors are becoming an increasingly mature technology, their operation is currently limited to a few research groups with low-temperature expertise. To broaden the use of these detectors in synchrotron applications, we have built a cryostat that attains the required

operating temperatures below ~ 0.5 K at the push of a button without the use of cryogenic liquids. The instrument was designed in collaboration between the Advanced Detector Group at Lawrence Livermore National Laboratory and VeriCold Technologies, and was built by VeriCold (figure 3). Like earlier cryogenic microcalorimeter X-ray spectrometers, it uses a pulse-tube refrigerator for precooling to ~ 3 K, and a two-stage adiabatic demagnetization refrigerator for cooling to its base temperature below 0.1 K [13]. The design incorporates elements like the cold finger and the preamplifier from an earlier STJ spectrometer based on liquid N_2 and He precooling that has been in operation at the Advanced Light Source synchrotron since 2000 [14]. It improves upon that design by removing the need for cryogenic liquids, and by increasing reliability and hold time at low temperature.



Fig. 3. Photograph of the STJ spectrometer. The detector is held at the end of the cold finger, and the preamplifiers are mounted in the shielded enclosure on the opposite side of the cryostat. The cylinder on top of the cryostat contains the gas reservoir of the pulse tube refrigerator, and compressor and rotary valve are separated from the cryostat to reduce vibrations.

A. Two-stage pulse tube refrigerator

Precooling to a temperature of $\sim 3 - 4$ K is achieved with a two-stage pulse tube refrigerator (PTR) [15, 16]. Like Stirling or Gifford-McMahon cryocoolers, pulse tube refrigerators use the compression and expansion of He gas to achieve cooling. The main advantage of PTRs is that their mechanically vibrating parts such as the rotary valve can be separated from the cold head. This greatly reduces the vibrations at the low-temperature detector stage and the associated microphonic noise. The main disadvantage of PTRs is their comparably low efficiency, which makes them less attractive for space-based applications, but matters little for synchrotron science.

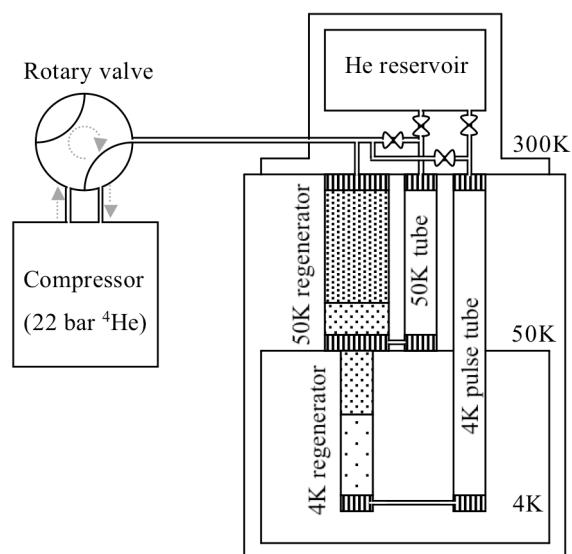


Fig. 4. Schematic of two-stage pulse tube refrigerator [16]. The heat exchangers (vertical lines) release heat to the environment at the top, and cool the load at the bottom during the periodic pressure cycles of the ^4He gas.

The compressor produces periodic gas pressure variations at a frequency of a few Hz set by the rotary valve. Pulse tube refrigerators consist of two columns, one of them (the “pulse tube”) being empty, and one of them (the “regenerator”) filled with porous solids (figure 4). In the regenerator and in the heat exchangers on top and at the bottom of the pulse tube, the gas is thermally well coupled to its environment, while the gas inside the pulse tube is thermally isolated and its temperature therefore varies with pressure.

During the high-pressure phase, the compressor moves pressurized He gas into the regenerator and the pulse tube at a temperature >300 K, which is cooled to ~ 300 K in the heat exchangers and the He reservoir on top of the pulse tube. During the low-pressure phase, the gas enters the pulse tube from the reservoir at ~ 300 K, cools as it expands, and cools the heat exchanger to a temperature <300 K as it enters the bottom of the regenerator. This cooling process is repeated at the frequency of the rotary valve. As long as there is no turbulent gas flow inside the pulse tube, equilibrium is established with the bottom of the pulse tube significantly below room temperature.

The base temperature of the PTR is determined by the quality of the regenerators, which must satisfy the conflicting requirements of good heat exchange and high He flow rate. For the 50 K regenerator, we use stainless steel and phosphor bronze screens, as well as small lead spheres in the lower section. For the 4 K regenerator we use small Pb and ErNi spheres [16]. The orifices between the pulse tubes and the He reservoir, and between the pulse tube and the rotary valve, produce a phase shift between gas compression and gas flow that limits the injection of hot He gas into the pulse tube. Their constriction is optimized for maximum cooling power at a valve frequency of ~ 2 Hz. Without load, this pulse tube refrigerator attains a base temperature of ~ 2.5 K with a power consumption of ~ 6.5 kW set by the Leybold Coolpak 6200 compressor.

B. Two-stage adiabatic demagnetization refrigerator

Cooling below the PTR base temperature of ~ 3 K is achieved by isothermal magnetization and adiabatic demagnetization of paramagnetic materials. Adiabatic demagnetization refrigerators (ADRs) consist of paramagnetic materials that are coupled to a cold bath, in this case the PTR cold stage at ~ 3 K, through a heat switch. An externally applied magnetic field aligns the spins of the paramagnets and lowers their entropy, and the associated heat of magnetization is carried into the cold bath through the closed heat switch. When the system is equilibrated at the PTR cold stage temperature of ~ 3 K, the heat switch is opened to decouple the paramagnets from the PTR. As the magnetic field is lowered slowly, i.e. “adiabatically”, keeping the entropy constant, the paramagnets cool the detector cold stage by absorbing heat in their spin system (figure 5).

Mathematically, the process of adiabatic demagnetization can be described by considering the entropy S of n ideal non-interacting spins with angular momentum J at a temperature T and magnetic field B :

$$\frac{S(T, B)}{nk_B} = x \coth(x) - (2J+1)x \coth((2J+1)x) + \ln \left(\frac{\sinh((2J+1)x)}{\sinh(x)} \right) \quad (2)$$

with $x = \mu_B g B / 2k_B T$

Here k_B is the Boltzmann constant, μ_B is the Bohr magneton, and g is the Landé g -factor. For real materials, interactions between neighboring spins produce a residual internal field B_{int} . This causes magnetic ordering at very low temperatures, and is accounted for by substituting $B \rightarrow (B^2 + B_{\text{int}}^2)^{1/2}$ in equation (2).

Modern ADRs often use a nested two-stage design to allow operation with from a starting temperature of ~ 3 to 4.2 K [17]. Gadolinium gallium garnet $\text{Gd}_3\text{Ga}_5\text{O}_{12}$ (GGG) is an attractive material for the primary (guard) stage because of its high heat capacity, its high thermal conductivity, and its magnetic ordering temperature of ~ 380 mK [18]. The GGG stage supports a second (detector) stage that uses paramagnetic $\text{Fe}(\text{NH}_4)(\text{SO}_4)_2 \times 12 \text{H}_2\text{O}$, commonly known as FAA for ferric ammonium alum. FAA has a very low ordering temperature of ~ 26 mK, which sets the minimum temperature the ADR can cool down to, although its low heat capacity requires the use of the GGG guard stage to reduce the heat load [19]. The material properties of FAA and GGG are summarized in table 1, and their entropies at $B = B_{\text{int}}$ and $B = 6.5$ T and their evolution during an ADR cooling cycle are shown in figure 5.

We operate both paramagnets with a single superconducting 6.5 T magnet and a single heat switch. The heat switch is electrically controlled with a stepper motor inside the ADR vacuum to avoid air leakage at O-ring sealed feedthroughs.

TABLE I

PROPERTIES OF PARAMAGNETIC MATERIALS FOR ADRS

Paramagnetic Material	Spin J	Landé g -factor	Internal Field B_{int} [T]	Ordering Temp. T_c [K]
GGG	7/2	2	0.48	380 mK
FAA	5/2	2	0.038	26 mK

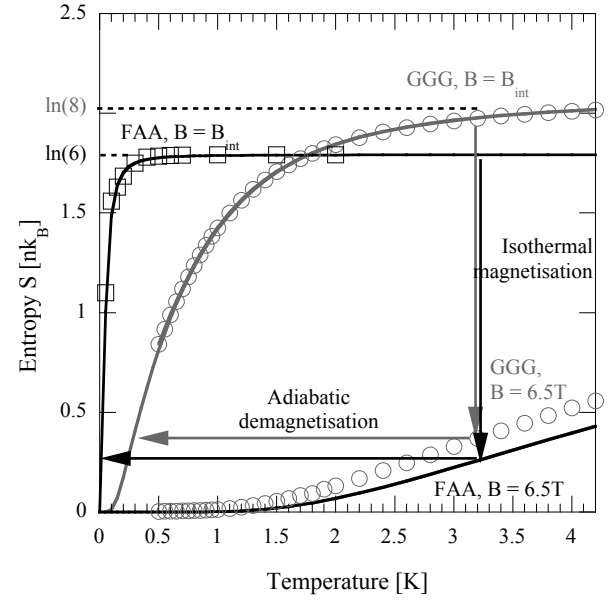


Fig. 5. Low-temperature entropy of ferric ammonium alum (FAA, black, squares) and gadolinium gallium garnet (GGG, grey, circles). The solid lines are theoretical values according to equation (2) with material constants from table (1). The arrows show the evolution of the entropy during an ADR cycle.

C. Cryostat performance

The entire cryostat cooldown is automated and takes ~ 15 - 18 hours (figure 6). The ADR cycle uses a magnetizing current of 36 A, and can be programmed ahead of time when the pulse tube has reached a temperature below 4 K.

Without regulation, the ADR attains a base temperature of ~ 28 mK, in agreement with the ordering temperature of 26 mK for the FAA paramagnet according to table (1). The GGG guard stage equilibrates around 380 mK, although this number depends somewhat on the initial temperature of the demagnetization cycle, as expected from figure 5. The cryostat base temperature is much lower than the ~ 0.3 to ~ 0.5 K required for STJ operation. We therefore use a small current in the ADR magnet to regulate the detector stage to the desired temperature. For an operating temperature of 0.3 K, the hold time between ~ 1 hour demagnetization cycles is ~ 72 hours with 128 signal wires connected to the STJ detector stage.

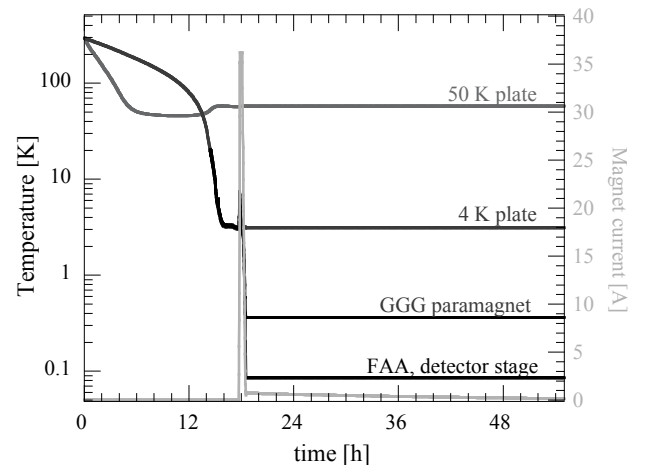


Fig. 6. Cooldown cycle of the pulse-tube ADR for regulation at 0.1 K

IV. SPECTROSCOPY

A. X-ray absorption spectroscopy

One application for STJ X-ray spectrometers is to characterize the chemistry of dilute samples by fluorescence-detected X-ray absorption spectroscopy (XAS) at synchrotron light sources. In these experiments, elemental energy levels are sampled with natural-linewidth-limited resolution by scanning the energy of a monochromatic X-ray beam across the binding energy of the element of interest, and measuring the X-ray absorption as a function of energy. Details of the absorption fine structure, which corresponds to transitions from a core level into the empty bound orbitals just above the Fermi energy, are indicative of the element's oxidation state, its bonding symmetry and the ligand field strengths. For concentrated samples, the electron yield is typically recorded as a measure of the absorption. For dilute samples, the sensitivity is highest if the subsequent fluorescence signal is recorded as a measure of the absorption, provided an X-ray detector is used that can separate the weak fluorescence of interest from the X-ray background due to the other elements in the sample [20]. STJs are advantageous in the soft X-ray band where Si(Li) and Ge detectors lack energy resolution and gratings lack detection efficiency [21].

Here we illustrate the potential of STJ spectrometers for material science at the synchrotron.

B. X-ray absorption spectroscopy and scintillators

Scintillators, i. e. materials that convert the energy of high-energy radiation into optical photons, are widely used in gamma spectroscopy. Despite years of research, the first scintillator ever found, thallium-doped sodium iodide, NaI:Tl [22], is still the most common scintillator material, because it can be grown cheaply and in large crystals, has a high optical light yield of $\sim 40,000$ photons/MeV, and offers reasonable absorption efficiency (density 3.67 g/cm^3), decay time (230 ns) and energy resolution ($\sim 6\%$ at 662 keV). Although NaI:Tl is hygroscopic and must therefore be sealed, it is widely used in nuclear medicine, environmental monitoring, geophysics and nuclear analysis.

In recent years, the family of lanthanum halides, and specifically cerium-doped lanthanum bromide, $\text{LaBr}_3\text{:Ce}$, has received wide attention because its high light yield of $>60,000$ photons/MeV, high efficiency (density 5.29 g/cm^3), an energy resolution as good as 2.6% at 662 keV and its fast decay time of $\sim 30 \text{ ns}$ [23]. Unfortunately, $\text{LaBr}_3\text{:Ce}$ is also moisture sensitive, like NaI:Tl, and is intrinsically radioactive due to primordial ^{138}La (table 2).

TABLE II
PROPERTIES OF SELECTED SCINTILLATOR MATERIALS

Material	Light yield [MeV ⁻¹]	Energy resolution at 662keV	Density [g/cm ³]	Decay time [ns]	Radioactive or hygroscopic?
NaI:Tl	40,000	6%	3.67	380	no / yes
$\text{LaBr}_3\text{:Ce}$	61,000	2.6%	5.29	30	yes / yes
$\text{SrI}_2\text{:Eu}$	100,000	2.8%	4.55	1200	no / yes

It now appears that europium-doped strontium iodide [24], $\text{SrI}_2\text{:Eu}$, offers an even higher light yield of $>100,000$ photons/MeV. Its energy resolution of 2.8% at 662 keV is comparable with $\text{LaBr}_3\text{:Ce}$, and could ultimately be better because of a lower non-proportionality in the response [25-27]. In addition, it does not contain intrinsically radioactive isotopes, and can be grown easily. This makes $\text{SrI}_2\text{:Eu}$ extremely attractive for gamma spectroscopy, especially in applications where its comparably slow decay time constant of $\sim 1.2 \mu\text{s}$ does not limit the data acquisition rate. To understand the ultimate limits that this recently re-discovered material may attain in gamma spectrometers, it is important to measure the properties that determine its performance.

One of these properties is the chemical state of the Eu dopants in the SrI_2 matrix. Many scintillators, including NaI:Tl and $\text{LaBr}_3\text{:Ce}$ rely on doping to create luminescence centers for high light output. These activator dopants form bound states inside the bandgap of the scintillator matrix, which trap the electron-hole pairs produced by gamma-absorption and emit scintillation photons upon relaxation. Usually only one of the oxidation states of these dopants is optically active. For europium, only divalent Eu^{2+} produces diople-allowed fast luminescence, while the decay in Eu^{3+} is dipole-forbidden and therefore very slow, of order $\sim \text{ms}$. This makes measurements of the Eu oxidation state important for scintillator optimization.

X-ray absorption spectroscopy (XAS) on activator ions by fluorescence detection with STJ detectors is a powerful method to determine dopant oxidation states, because it can quantify oxidation states with a precision of a few percent for typical activator concentrations in the $\sim 1000 \text{ ppm}$ range [28, 29]. XAS in the soft X-ray band is often preferred over the more common hard X-ray spectroscopy, because natural linewidths are narrower at low energy and therefore more sensitive to chemical shifts [30].

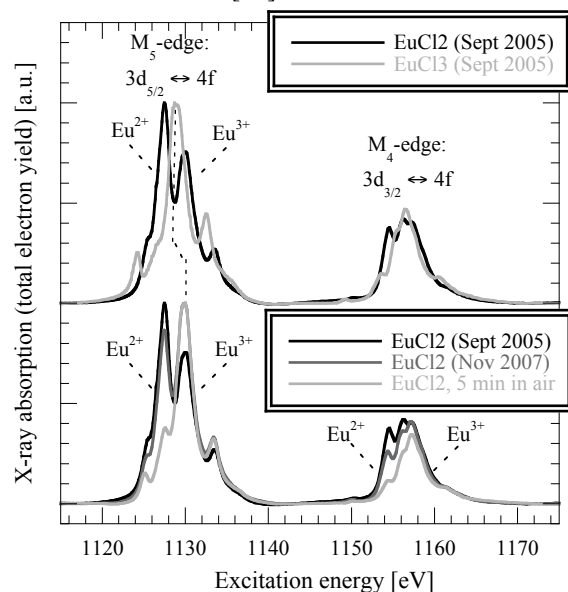


Fig. 7. X-ray absorption spectra at the $M_{4,5}$ -edges of divalent EuCl_2 and trivalent EuCl_3 model compounds show strong chemical shifts for different Eu valences. Note that the less stable EuCl_2 converts to Eu^{3+} on exposure to air.

C. X-ray absorption spectroscopy at the Eu $M_{4,5}$ -edges

Figure 7 shows XAS spectra of two europium reference compounds to illustrate the power of XAS for chemical analysis. They are acquired at beam line 4.0.2 at the Advanced Light Source (ALS) synchrotron in Berkeley, CA. The commercial EuCl_2 and EuCl_3 powder samples are prepared in a glove box with an oxygen concentration <1 ppm, and mounted on double-sided carbon tape in a capped sample holder that is only uncapped inside the UHV measurement chamber. The excitation energy of the incident X-ray beam is scanned across the binding energy of the europium $3d_{5/2}$ and $3d_{3/2}$ energy levels, and the corresponding M_5 and M_4 X-ray absorption edges are measured by total electron yield with a Channeltron[®] electron multiplier. The spectra are normalized by the incident beam intensity and, after background subtraction, set to unity at the strongest absorption feature. The energy is calibrated by setting the energy of the dominant peak of Eu^{2+} at the M_5 -edge to 1127.5 eV. The monochromator resolution is 0.2 eV, well below the natural linewidth of the $3d \rightarrow 4f$ transitions at the Eu $M_{4,5}$ -edges.

Figure 7 (top) shows clear chemical shifts and differences in XAS fine structure between the Eu sites in trivalent EuCl_3 and in divalent EuCl_2 . The absorption edges in EuCl_3 lie at higher energy (1128.9 eV and 1156.5 eV) than in EuCl_2 (1127.5 eV and 1154.5 eV), because higher oxidation states imply a lower electron density at the Eu sites, which reduces the screening of the core electron levels. This leads to tighter binding energies for the Eu $3d_{5/2}$ and $3d_{3/2}$ core levels and thus shifts the M_5 and M_4 absorption edges to higher energy.

The EuCl_2 spectrum exhibits additional high energy features at 1130.0 eV and 1133.5 eV in the M_5 -edge, and at 1157.3 eV in the M_4 -edge. These edge features are not characteristic of Eu^{2+} [31], but indicate that some of the less stable Eu^{2+} has been converted to Eu^{3+} during several years of storage, even in a nominally inert atmosphere. This is supported by the observation that the XAS spectrum of the same EuCl_2 powder has changed between September 2005 and November 2007, with the fraction of the less stable Eu^{2+} decreasing and that of Eu^{3+} increasing (figure 7, bottom). To confirm that these higher-energy features are in fact due to Eu^{3+} , we have exposed the EuCl_2 sample for 5 minutes to air in the load lock of the UHV chamber, and taken another spectrum on the same specimen. The absorption peak at 1127.5 eV has almost completely disappeared, indicating that most of the Eu^{2+} has been consumed. Further exposure to air no longer changes the XAS spectrum.

Note that the edge energies for the oxidized EuCl_2 are at 1130.0 and 1133.5 eV, somewhat *above* the edge energies of 1128.9 and 1132.5 eV in EuCl_3 , although both compounds likely contain europium in the same trivalent oxidation state. This is because oxidation in air forms europium oxide Eu_2O_3 or europium oxychloride EuOCl , and oxygen has a higher electronegativity than Cl. This means that the electron density at the Eu ions is lower in Eu_2O_3 or EuOCl than in EuCl_3 , and the associated edge energies are therefore higher. It shows that X-ray absorption spectra are not only sensitive to oxidation states, but also to ligand field strengths.

D. Spectroscopy on Eu dopants in SrI_2

X-ray absorption spectroscopy can also be used to characterize Eu dopants in SrI_2 , except that the low Eu concentration in SrI_2 necessitates the use of a fluorescence detector to separate the weak Eu M fluorescence from the X-ray background of the scintillator matrix. To illustrate the power of fluorescence-detected XAS for scintillator analysis, we show a Eu $M_{4,5}$ -edge spectrum of an early SrI_2 sample before growth process optimization. Single crystals of SrI_2 are grown from anhydrous alkaline- and rare-earth halides by the vertical Bridgman technique in evacuated silica ampoules [26], and afterwards examined only inside glove boxes and stored under oil between experiments. To remove possible surface oxides, the sample is polished in a glovebox with an oxygen concentration <1 ppm, and mounted on a double-sided carbon tape inside a capped sample holder that is also only uncapped inside the UHV measurement chamber. The excitation energy of the synchrotron X-ray beam is scanned across the binding energy of the Eu $3d_{5/2}$ and $3d_{3/2}$ levels, and a full X-ray fluorescence spectrum is taken with each STJ detector at each excitation energy. Windows are set around the europium M X-ray fluorescence (XRF) signal to separate it from the matrix background, and the intensity of this XRF signal is recorded as a measure of the absorption. The signal is normalized by the intensity of the incident beam, and set to unity at the strongest absorption feature.

Figure 8 shows the Eu $M_{4,5}$ -edges of the polished $\text{SrI}_2\text{:Eu}$ sample (solid grey spectrum). Two edge peaks are visible, clearly separated by 3.4 eV, suggesting that the sample contains both Eu^{2+} and Eu^{3+} . This is surprising, because this scintillator sample has already shown an exceptionally high light yield of 80,000 photons/MeV for an integration time of 3 μs that would suggest a small fraction of the slow-decaying Eu^{3+} . We have therefore repeated the experiment on the same sample, this time cleaving the SrI_2 single crystal in the oxygen-

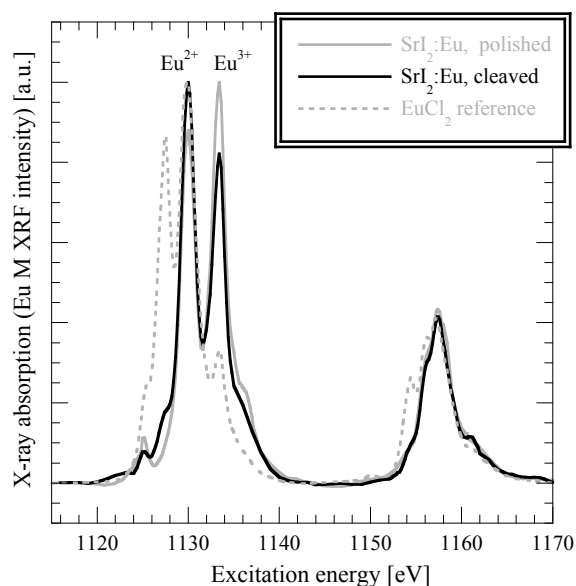


Fig. 8. Fluorescence-detected X-ray absorption spectrum of Eu dopants in $\text{SrI}_2\text{:Eu}$. The different Eu speciation in the polished and the cleaved sample indicates difficulties of preparing a pristine SrI_2 sample.

free glovebox and mounting it on a double-sided carbon tape inside a capped sample holder such that only the fresh surface is exposed to the synchrotron beam during the measurements. The energy is calibrated by examining a EuCl_2 sample before the $\text{SrI}_2\text{:Eu}$ scintillator scan and setting the Eu^{2+} peak of its M_5 -edge to 1127.5 eV (figure 8, dashed grey scan). Again, two peaks are visible for the cleaved $\text{SrI}_2\text{:Eu}$ scintillator (figure 8, solid black scan), but their ratio is changed. This demonstrates that the two peaks do in fact originate from the two different Eu species Eu^{2+} and Eu^{3+} , and that cleaving produces a sample with a higher Eu^{2+} content that is more representative of the bulk properties of this $\text{SrI}_2\text{:Eu}$ sample. Still, the presence of Eu^{3+} is unexpected given the high light yield of $>80,000$ photons/ MeV for this sample. It may indicate that future improvements in light yield are possible if all Eu is converted to Eu^{2+} . Alternatively, it may indicate that sample preparation in a glove box and loading in a capped sample holder, while usually sufficient, may not fully prevent oxidation in the case of Eu^{2+} . This has been observed before in divalent Eu species, even in nominally inert atmospheres [32], and may have occurred in our experiments during sample transport between the glovebox and the UHV chamber. While the capped sample holder is sealed inside the glovebox, there is a possibility that residual water or oxygen were adsorbed on the cap, the O-ring seal or the carbon tape which may have oxidized the SrI_2 sample.

We observe that the M_5 -edge energy of 1130.0 eV for Eu^{2+} in $\text{SrI}_2\text{:Eu}$ is *above* that for EuCl_2 (1127.5 eV), which would typically indicate that the electron density at the Eu site is lower in $\text{SrI}_2\text{:Eu}$ than in EuCl_2 , despite the nominally identical +2 oxidation state. This is surprising, since Sr is 7-coordinated to the I-ions in SrI_2 with an average nearest-neighbor distance of 3.35 Å [32], while Eu is 9-coordinated in EuCl_2 with a nearest-neighbor distance of 2.5 Å to the Cl ions [31]. Assuming Eu occupies an Sr site in SrI_2 , it should also be 7-coordinated with I at a similarly long distance to its nearest neighbors, and since the electronegativity of I is less than the electronegativity of Cl, the electron density at Eu should be higher in the SrI_2 matrix than in EuCl_2 . This should lead to a lower Eu M_5 -edge energy, which is not observed. Further research is necessary to better understand the Eu chemistry and distinguish which fraction of Eu^{3+} is intrinsic to the $\text{SrI}_2\text{:Eu}$ crystal growth, and which fraction is formed during XAS sample preparation.

Still, these measurements show the extreme sensitivity of XAS with STJ detectors to measure speciation and bonding environment of dilute activators. They also indicate that the Eu speciation in SrI_2 is rather subtle and not always stable.

V. SUMMARY

We have built a cryostat for superconducting tunnel junction (STJ) soft X-ray detector operation at the synchrotron that attains the required operating temperature below 0.5 K without the use of liquid cryogens. It uses a two-stage pulse-tube refrigerator for precooling to ~ 3 K, and a two-stage adiabatic demagnetization refrigerator (ADR) to attain a base temperature of 28 mK. It is equipped with 128 signal wires to

the low-temperature detector stage so that it can eventually house STJ detector arrays with more than 100 pixels. In this configuration the cryostat has a hold time of >72 hours between 1-hour demagnetization cycles for temperature regulation at a typical STJ operating temperature of 0.3 K. The STJ spectrometer is designed to measure chemical speciation of dilute samples by high-resolution soft X-ray spectroscopy at the synchrotron.

We have also demonstrated the utility of fluorescence-detected X-ray absorption spectroscopy (XAS) to characterize europium activators in $\text{SrI}_2\text{:Eu}$ scintillator materials. The spectra show a mixture of Eu^{2+} and Eu^{3+} , which changes sensitively with XAS sample preparation. At present, we cannot yet distinguish which fraction of the optically inactive Eu^{3+} is generated during crystal growth, and which fraction is produced during sample preparation. In either case, SrI_2 is already emerging as one of the highest resolution scintillator materials ever found, and XAS with STJs is a powerful method to characterize the oxidation state and bonding configuration of its europium activator ions to better control scintillator growth chemistry for optimized light yield and energy resolution.

REFERENCES

- [1] For an overview of recent developments in the field of cryogenic detectors, see the proceedings of the 12th International Workshop of Low Temperature Detectors (LTD-12), published as *J. Low Temp. Phys.*, vol. 151, 2008
- [2] S. Friedrich, "Cryogenic X-ray detectors for synchrotron science", *J. Synch. Rad.*, vol. 13, pp. 159-171, 2006
- [3] M. Kurakado, "Possibility of High Resolution Detectors Using Superconducting Tunnel Junctions", *Nucl. Inst. Meth.*, vol. 196, pp. 275-277, 1982
- [4] N. E. Booth, "Quasiparticle Trapping and the Quasiparticle Multiplier", *Appl. Phys. Lett.*, vol. 50, pp. 293-295, 1987
- [5] C. A. Mears, S. E. Labov, A. T. Barfknecht, "Energy-Resolving Superconducting X-Ray Detectors with Charge Amplification Due to Multiple Quasiparticle Tunneling", *Appl. Phys. Lett.*, vol. 63, pp. 2961-2963, 1993
- [6] K. Segall, C. Wilson, L. Frunzio, L. Li, S. Friedrich, M. C. Gaidis, D. E. Prober, A. E. Szymkowiak, S. H. Moseley, "Noise Mechanisms in Single-Photon Superconducting Tunnel Junction Detectors", *Appl. Phys. Lett.*, vol. 76, pp. 3998-4000, 2000
- [7] M. Frank, L.J. Hiller, J.B. LeGrand, C.A. Mears, S.E. Labov, M.A. Lindeman, H. Netel, D. Chow, A.T. Barfknecht, "Energy Resolution and High Count Rate Performance of Superconducting Tunnel Junction X-Ray Spectrometers", *Rev. Sci. Instr.*, vol. 69, pp. 25-31, 1998
- [8] S. Friedrich, A. Vailionis, O. Drury, T. Niedermayr, T. Funk, W. N. Kang, E. M. Choi, H. J. Kim, S. I. Lee, S. P. Cramer, C. Kim, S. E. Labov "A Multichannel Superconducting Tunnel Junction Detector for High-Resolution X-ray Spectroscopy of Magnesium Diboride Films", *IEEE Trans. Appl. Supercond.*, vol. 13, pp. 1114-1119, 2003
- [9] J. B. LeGrand, C. A. Mears, L. J. Hiller, M. Frank, S. E. Labov, H. Netel, D. Chow, S. Friedrich, M.A. Lindeman, "A Superconducting Tunnel Junction X-Ray Detector with Performance Limited by Statistical Effects", *Appl. Phys. Lett.*, vol. 73, pp. 1295-1297, 1998
- [10] P. Verhoeve, "Photon Counting Low Temperature Detectors for Visible to Gamma Ray Astrophysics", *J. Low. Temp. Phys.*, vol. 151, pp. 675-683, 2008
- [11] G. Angloher, P. Hettl, M. Huber, J. Jochum, F. v. Freilitzsch, R. L. Mößbauer, "Energy resolution of 12 eV at 5.9 keV from Al-superconducting tunnel junction detectors", *J. Appl. Phys.*, vol. 89, pp. 1425-1527, 2001
- [12] J. Halbritter, M. Grundner, "XPS and AES studies on oxide growth and oxide coatings on niobium", *J. Appl. Phys.*, vol. 51, pp. 397-405, 1980

- [13] B. Simmnacher, R. Weiland, J. Hoehne, F. v. Freilitzsch, C. Hollerith "Semiconductor Material Analysis Based on Microcalorimeter EDS", *Microelectronics Reliability*, vol. 45, pp. 1675-1680, 2003
- [14] S. Friedrich, T. Niedermayr, O. Drury, M.F. Cunningham, M.L. van den Berg, J. N. Ullom, A. Loshak, T. Funk, S. P. Cramer, J. D. Batteux, E. See, M. Frank, S. E. Labov, "A superconducting Detector Endstation for High-resolution energy-dispersive SR-XRF", *Nucl. Inst. Meth. A*, vol. 467, pp. 1117-1120, 2001
- [15] E. I. Mikulin, A. A. Tarasov, M. P. Shkrebyonok, "Low-temperature expansion pulse tubes", *Adv. Cryo. Eng.*, vol. 31, pp. 629, 1984.
- [16] C. Wang, G. Thummes, C. Heiden, "A two-stage pulse tube cooler operating below 4 K", *Cryogenics*, vol. 37, pp. 159-164, 1997
- [17] C. Hagmann, P. L. Richards "Two-stage magnetic refrigerator for astronomical applications with reservoir temperatures above 4K", *Cryogenics*, vol. 34, pp. 221-226, 1994
- [18] E. W. Hornung, R. A. Fisher, G. E. Brodale, W. F. Giauque, "Magneto-hydrodynamics of gallium gadolinium garnet. II. Heat capacity, entropy, magnetic moment from 0.5 to 4.2 K, with fields to 90 kG, along the [111] axis", *J. Chem. Phys.*, vol. 61, pp. 282 - 291, 1974
- [19] O. E. Vilches, J. C. Wheatley, "Measurements of the specific heats of three magnetic salts at low temperatures" *Phys. Rev.*, vol. 148, pp. 509 - 516, 1966
- [20] J. Jaklevic, J. A. Kirby, M. P. Klein, A. S. Robertson, G. S. Brown, P. Eisenberger, "Fluorescence-detection of EXAFS: Sensitivity Enhancement for dilute species and thin films", *Solid State Comm.*, vol. 23, pp. 679 -682, 1977
- [21] O. B. Drury, S. Friedrich, "Sensitivity and S/N-Ratio of Superconducting High-Resolution X-Ray Spectrometers", *IEEE Trans. Appl. Supercond.*, vol. 15, pp. 613-617, 2005
- [22] R. Hofstadter, "The detection of Gamma-Rays with Thallium-Activated Sodium Iodide Crystals", *Phys. Rev.*, vol 75, pp. 796 - 810, 1949
- [23] E. V. D. van Loef, P. Dorenbos, C. W. E. van Eijk, K. Kramer, H. U. Gudel, "High-energy-resolution scintillator: Ce^{3+} activated LaBr_3 ", *Appl. Phys. Lett.*, vol.79, pp. 1573-1575, 2001
- [24] R. Hofstadter, "Europium-activated Strontium Iodide Scintillators," US Patent 3,373,279 (1968)
- [25] N. J. Cherepy, G. Hull, A. D. Drobshoff, S. A. Payne, E. van Loef, C. M. Wilson, K. S. Shah, U. N. Roy, Arnold Burger, L. A. Boatner, W.-S. Choong, W. W. Moses, "Strontium and barium iodide high light yield scintillators", *Appl. Phys. Lett.* 92, pp. 083508, 2008
- [26] E. V. D. van Loef, C. M. Wilson N. J. Cherepy, G Hull, S. A. Payne, W. S. Choong, W. W. Moses, K. S. Shah, "Crystal Growth and Scintillation Properties of Strontium Iodide Scintillators", these proceedings.
- [27] N. J. Cherepy, S. Payne, G. Hull, J. Kuntz, J. Roberts, S. Asztalos, D. Manatt, A. Drobshoff, R. Sanner, T. Tillotson, S. Fisher, E.V.D. van Loef, C. Wilson, K. Shah, U. Roy, R. Hawrami, A. Burger, L. Boatner, W. S. Choong, W. W. Moses, "Scintillators with Potential to Supersede LaBr_3 ", these proceedings.
- [28] C. L. Melcher, S. Friedrich, M. A. Spurrier, S. P. Cramer, P. Szupryczynski, R. Nutt, "Cerium oxidation state in $\text{LSO}:\text{Ce}$ scintillators", *IEEE Trans. Nucl. Sci.*, vol 52, pp. 1809 - 1812, 2005
- [29] S. Friedrich, O. B. Drury, S. Yuan, P. Szupryczynski, M. A. Spurrier, C. L. Melcher, "A 36-Pixel Tunnel Junction Soft X-Ray Spectrometer for Scintillator Material Science", *IEEE Trans. Appl. Superconductivity*, vol. 17, pp. 351 - 354, 2007
- [30] O. B. Drury, S. Friedrich, S. J. George, S. P. Cramer, "The advantages of soft x-rays and of cryogenic spectrometers for chemical speciation measurements on dilute samples", *Nucl. Inst. Meth. A*, vol. 559, pp. 728 - 730, 2006
- [31] M. Mizumaki, Y. Saitoh, A. Agui, K. Yoshii, A. Fujimori, S. Nakamura, "XAS and MCD studies in $\text{Eu}_{0.6}\text{Sr}_{0.4}\text{MnO}_3$ ", *J. Synchrotron Rad.*, vol. 8, pp. 440 - 442, 2001
- [32] S. Watanabe, A. K. Adya, L. Rycerz, A. C. Barnes, M. Gaune-Escard, Y. Okamoto, H. Akatsura, H. Matsuura, "XAFS Study of Europium Chloride at High Temperatures", *Prog. Nucl. Energy*, vol. 47, pp. 632-638, 2005
- [33] E. T. Rietschel, H. Bärnighausen "Die Kristallstruktur von Strontium-jodid SrJ_2 ", *Z. Anorg. Allg. Chem.*, vol. 368, pp. 62-72, 1969